

A Quantum Key Distribution Testbed using a Plug&Play Telecom-wavelength Single-Photon Source

Timm Gao,¹ Lucas Rickert,¹ Felix Urban,¹ Jan Große,¹ Nicole Srocka,¹ Sven Rodt,¹
Anna Musiał,² Kinga Żołąńcz,³ Paweł Mergo,⁴ Kamil Dybka,⁵ Wacław Urbańczyk,³
Grzegorz Sęk,² Sven Burger,⁶ Stephan Reitzenstein,¹ and Tobias Heindel^{1, a)}

¹⁾*Institute of Solid State Physics, Technische Universität Berlin, 10623 Berlin, Germany*

²⁾*Department of Experimental Physics, Wrocław University of Science and Technology, 50-370 Wrocław, Poland*

³⁾*Department of Optics and Photonics, Wrocław University of Science and Technology, 50-370 Wrocław, Poland*

⁴⁾*Institute of Chemical Sciences, Maria Curie Skłodowska University, 20-031 Lublin, Poland*

⁵⁾*Fibrain Sp. z o.o., 36-062 Zaczernie, Poland*

⁶⁾*Zuse Institute Berlin, 14195 Berlin, Germany*

(Dated: 7 January 2022)

Deterministic solid-state quantum light sources are considered key building blocks for future communication networks. While several proof-of-principle experiments of quantum communication using such sources have been realized, most of them required large setups often involving liquid helium infrastructure or bulky closed-cycle cryotechnology. In this work, we report on the first quantum key distribution (QKD) testbed using a compact benchtop quantum dot single-photon source operating at telecom wavelengths. The plug&play device emits single-photon pulses at O-band wavelengths (1321 nm) and is based on a directly fiber-pigtailed deterministically-fabricated quantum dot device integrated into a compact Stirling cryocooler. The Stirling is housed in a 19-inch rack module including all accessories required for stand-alone operation. Implemented in a simple QKD testbed emulating the BB84 protocol with polarization coding, we achieve an antibunching of $g^{(2)}(0) = 0.10 \pm 0.01$ and a raw key rate of up to (4.72 ± 0.13) kHz using an external pump laser. In this setting, we further evaluate the performance of our source in terms of the quantum bit error ratios, secure key rates, and tolerable losses expected in full implementations of QKD also accounting for finite key size effects. Furthermore, we investigate optimal settings for a two-dimensional temporal acceptance window applied on receiver side, resulting in predicted tolerable losses up to 23.19 dB. Not least, we compare our results with previous proof-of-concept QKD experiments using quantum dot single-photon sources. Our study represents an important step forward in the development of fiber-based quantum-secured communication networks exploiting sub-Poissonian quantum light sources.

^{a)}Corresponding author: tobias.heindel@tu-berlin.de

I. INTRODUCTION

Quantum light sources emitting single- and entangled photon states on the push of a button are building blocks for advanced photonic quantum technologies and quantum communication in particular. They carry the potential to boost the performance of quantum key distribution (QKD) systems¹ and to enable secure communication at global scales by exploiting quantum repeater architectures². Among the several promising species of quantum emitters in the solid-state (see Refs.³⁻⁵ for detailed reviews), epitaxial semiconductor quantum dots (QD) stand out due to the highest reported single photon purity in terms of $g^{(2)}(0)$ ^{6,7}, high photon indistinguishability and brightness of single- and entangled-photon states⁸⁻¹⁰, and their speed enabling GHz clock rates^{11,12}. Due to a lack of efficient and practical quantum light sources, most implementations of QKD are still carried out with faint lasers¹³, referred to as weak coherent pulses (WCPs). To compensate for the resulting multi-photon contributions, so-called decoy-state protocols have been invented^{14,15}, which define the current state-of-the-art in direct point-to-point QKD¹⁶. Still, due to their Poissonian light-states, WCP-based implementations are fundamentally limited in their efficiency. From the tremendous progress seen in the field of QD-based quantum light sources, however, renewed prospects arise for real-world implementations of quantum communication benefitting from sub-Poissonian light states.

While previously the performance and yield of QD-based nanophotonic devices was limited by the random spatial distribution of the quantum emitters and the inhomogeneous spectral broadening of the emitter ensemble (both resulting from the stochastic nature of the self-assembly process during epitaxial growth), nowadays deterministic fabrication technologies enable much higher degrees of control. Exploiting marker-based¹⁷ or in-situ^{18,19} lithography techniques, photonic microstructures can be fabricated deterministically around single pre-selected emitters resulting in high performance and high yield of devices (e.g. Refs.²⁰⁻²²). The advancements of deterministic fabrication technologies, as summarized in a recent review article²³, are expected to have large impact on the application of deterministic quantum light sources in photonic quantum technologies and are also a key to the results reported in our work.

Moreover, QD-based sources demonstrated their potential for quantum communication in several proof-of-principle experiments using single-photon²⁴⁻²⁹ and entangled-photon³⁰⁻³²

states. We refer the interested reader to Ref.³³ for an extensive recent review article on implementations of quantum communication using QDs. For the remainder of this article, we consider the first QKD protocol ever invented, known as BB84³⁴. Here, one party, Alice, sends single photons randomly prepared in four different polarization states (spanning two conjugate bases) via the quantum channel to the second party, Bob, who detects the photons randomly and independent of Alice in the two different polarization bases. Assuming a single-photon source (SPS) with ideal photon statistics ($g^{(2)}(0) = 0$), the key parameters to consider in this prepare-and-measure configuration are the sifted key rate, the quantum bit error rate (QBER), and the secure key rate. The sifted key refers to the fraction of the transmitted (and detected) raw key after excluding (i.e. sifting) the bits prepared and measured in different polarization basis (resulting in a probabilistic projection). The QBER quantifies the amount of erroneous bits in the sifted key and determines how much the sifted key needs to be shrunk in the classical post-processing (error correction and privacy amplification), which results finally in the secure key rate usable for data encryption. If the SPS has a finite $g^{(2)}(0)$, which is always the case in practical implementations, a finite multi-photon emission probability needs to be further taken in to account in the security analysis¹. In addition, one distinguishes scenarios assuming that an infinitely long key can be generated, corresponding to the so-called asymptotic limit, and more realistic scenarios taking finite-key size effects into account³⁵.

Despite the immense progress in the field, the need for large optical setups and bulky cryotechnology, involving liquid helium infrastructure or complex closed-cycle refrigerators, is often considered a major drawback of QDs or other types of "cryogenic" emitters if it comes to applications. On the other hand, the advances in the performance of QD-based quantum light sources and the prospects for device integration triggered the interest in developing more practical user-friendly sources for applications outside shielded laboratories. First efforts in this direction utilized fiber-coupled QD samples employing fiber-bundles containing about 600 individual fiber cores to spatially post-select a single emitter³⁶. More recently, the direct fiber-coupling of photonic nanostructures with embedded QDs, such as photonic wires³⁷ and optically³⁸ as well as electrically³⁹ pumped micropillar cavities, has been reported. Still, these efforts relied on conventional bulky cryotechnology. In previous work, our groups pioneered and advanced the integration of QD-devices in Stirling cryocoolers for stand-alone operation⁴⁰⁻⁴², enabling much more compact setups. Applications of these

user-friendly sources in implementations of quantum information, however, have not been demonstrated so far.

In this article, we report on the application of a benchtop plug&play QD-SPS operating at telecom wavelengths in experimental tests for quantum communication. To this end, the outline of our article is as follows: In Section II we first present the overall QKD-testbed used to emulate the BB84 protocol for the studies in this work before providing details on the transmitter- and receiver-module in distinct subsections. Subsection II A presents the developed benchtop QD-SPS providing push-button single-photon pulses in a standard Telecom fiber and provide a basic characterization of its spectral and quantum-optical properties. The receiver-module is discussed in Subsection II B. Section III discusses the experimental results achieved with our QKD testbed. Here, we start with a basic performance evaluation in Subsection III A quantifying the achievable QBER, the suppression of multi-photon emission events via $g^{(2)}(0)$, and the mean photon number per pulse μ . In Subsection III B, we analyze the achievable secure key rates, both in the asymptotic and finite-key size regime. We apply temporal filtering to optimize the achievable performance and to maximize the tolerable transmission loss, i.e. transmission distance. The results obtained are discussed and compared with previous implementations of QKD in Subsection III C. Our article closes with a summary and an outlook in Section IV.

II. QUANTUM KEY DISTRIBUTION TESTBED

The QKD testbed developed for the studies in this work is illustrated in Fig. 1(a). On the transmitter side, Alice comprises a benchtop optically triggered source of flying qubits operating in the telecom O-band. Here, single-photon pulses are provided via a standard Telecom fiber and generated inside a 19 inch rack module housing all components required for this complex task, including a cryocooler, a pump laser, and a spectral filter. This benchtop source module enables cryogenic operation, by integrating a deterministically-fabricated fiber-pigtailed QD-device into a compact Stirling cryocooler. Details on the transmitter module are provided in Section II A. To evaluate the performance of our quantum-light source for applications in quantum communication, we prepare single-photon pulses in four polarization states, required for implementations of the BB84 protocol, using a linear polarizer and a $\lambda/2$ waveplate. Note, while full implementations of QKD require a dynamic

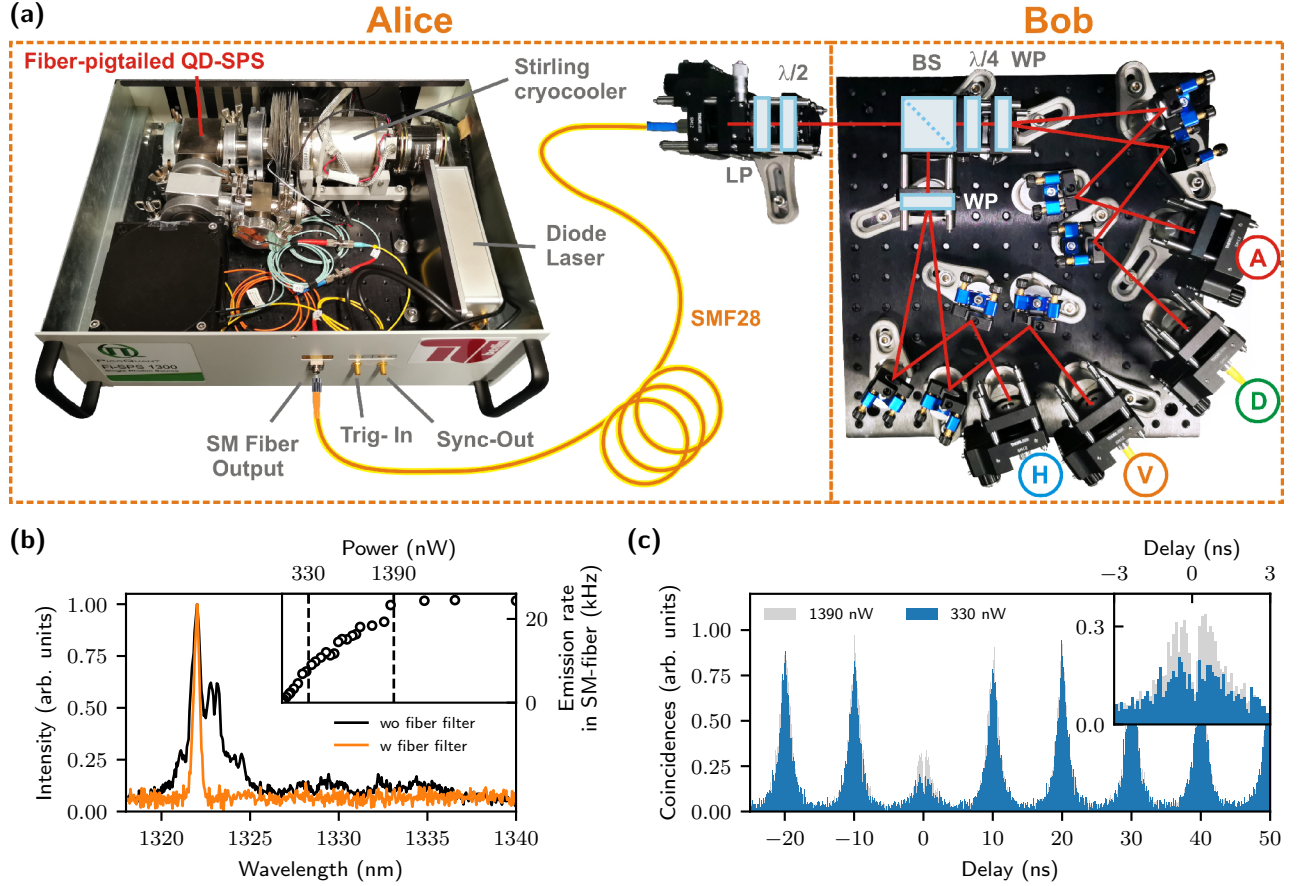


FIG. 1. BB84-QKD testbed using a compact stand-alone quantum dot (QD) single-photon source (SPS) integrated in a 19 inch rack-module and polarization encoding. (a) The transmitter Alice comprises a deterministically fiber-coupled QD-SPS integrated in a Stirling cryocooler, a pulsed diode-laser for excitation, and a fiber-based spectral filter (not shown in the image). Alice sends pulses with fixed polarization (H, V, D, A) set by a linear polarizer (LP) and a lambda-half ($\lambda/2$) waveplate to the receiver Bob. The latter consists of a 4-state polarization analyzer realized with a 50:50 beamsplitter (BS), a compensating λ -quarter ($\lambda/4$) waveplate, and two Wollaston-prisms (WP) for spatial separation of orthogonal polarizations. (b) Output spectra of the fiber-coupled SPS with (orange) and without (black) spectral filtering using a fiber-based bandpass filter set to a center wavelength of 1321 nm. Spectra were recorded at a temperature set-point of the Stirling cryocooler of 40 K. (c) Second-order autocorrelation $g^{(2)}(\tau)$ histogram under pulsed excitation at 785 nm with a repetition rate of 100 MHz using the internal laser (time-bin width: 100 ps). Depending on the excitation power (see inset), more or less pronounced recapture processes are observed near $\tau = 0$ due to the above-band excitation scheme.

modulation of the polarization states (e.g. via electro-optical modulators), we statically prepare the polarization states in sequential measurement runs in our testbed, which allows us to determine all key-parameters for QKD and their limits. The polarization qubits are then sent to the receiver module in a back-to-back configuration, i.e. without additional loss in the quantum channel. On the receiver side, Bob comprises a four- (4-) state polarization decoder designed for operation at Telecom wavelengths. Here, photons in the four BB84-states are decoded in four different output fibers connected to a 4-channel single-photon detection system. For details on the receiver module, we refer to Section II B.

A. Transmitter-Module (Alice)

At the heart of our transmitter module, the SPS comprises a single InGaAs/GaAs QD which was preselected and deterministically integrated into a photonic microstructure using 3D in-situ electron-beam lithography²⁰. The quantum emitter is embedded in a monolithic micromesa structure (height: 705 nm, diameter: 2 μ m) integrated on top of a distributed Bragg-reflector serving as bottom mirror (15×118 nm $\text{Al}_{0.92}\text{Ga}_{0.08}\text{As}$ and 102 nm GaAs) for increasing the photon collection efficiency. To shift the emission of the QDs in this sample to the telecom O-band, a strain-reducing InGaAs-layer was applied during the epitaxial growth via metal-organic vapor deposition (MOCVD)⁴³. For integration in the Stirling cryocooler (CryoTel GT, Sunpower Inc.), the QD-device is permanently coupled to a custom-made Ge-doped optical single-mode (SM) fiber with high numerical aperture ($\text{NA} = 0.42$), whose core is thermally expanded onto a standard SMF-28e fiber⁴⁴. The design parameters for the combined micromesa-fiber assembly follow results of numerical simulations based on finite-element methods⁴⁵ using an Bayesian optimization algorithm⁴⁶. The air-cooled linear-piston Stirling cryocooler with fiber-optical feedthroughs allows for cryogen-free operation of the SPS down to 40 K (at 100 W cooling power) while fitting into a 19-inch rack box. For optically pumping the quantum emitter, two different lasers can be coupled to the sample via a 1x2 SM fiber-coupler with a split ration of 90:10. While the laser emission reaches the sample via the 10 %-port, the sample emission is collected via the 90 %-port for further use. Two options are available for the laser source: (1) a compact diode laser with fixed wavelength for above-bandgap excitation (wavelength: 785 nm, pulsewidth: 70 ps, repetition rate: variable, PicoQuant GmbH) which is integrated in the 19-inch rack module,

or (2) an external spectrally-tunable laser system (pulsewidth: 2 ps, repetition rate: 80 MHz, APE GmbH) allowing for quasi-resonant excitation of the single quantum emitter (emission wavelength: 1321 nm) in an excited state (p-shell) at a wavelength of 1247.9 nm. Both lasers are coupled to SM fibers allowing for a simple connection to the 1x2 fiber-coupler inside the rack module. While option (1) is used for the pre-characterization of the SPS presented in this section (see further below), option (2) is used for the actual QKD tests in Section III, as quasi-resonant excitation enables an improved single-photon purity being beneficial in QKD. For high-transmission and compact spectral filtering, a fiber-based bandpass filter with adjustable center wavelength is used (full-width at half-maximum 0.5 nm, WL Photonics Inc.) is integrated in the 19-inch rack module, which removes spectral contributions of background emitters and residual scattered light of the excitation laser. Additionally, we applied polarization suppression to reduce the laser background.

Figure 1 (b) shows the spectral characteristic of our transmitter module at the SM-fiber output with and without fiber-based bandpass filter, respectively, using the integrated diode laser triggering at a clock rate of 100 MHz. The corresponding second-order autocorrelation histogram $g^{(2)}(\tau)$ recorded at the spectrally filtered output signal, is shown in Fig. 1 (c) for excitation powers of the quantum emitter at (1390 nW) and well below (330 nW) saturation, respectively. For this pre-characterization measurement, a standard fiber-coupled Hanbury-Brown and Twiss setup was used in combination with superconducting nanowire single-photon detectors (SNSPDs) (Single Quantum Eos, Single Quantum BV) with a temporal resolution between 35 ps and 100 ps. Analyzing the raw measured coincidences within the full repetition period, we extract antibunching values of $g^{(2)}(0) = 0.49 \pm 0.01$ at saturation and $g^{(2)}(0) = 0.37 \pm 0.02$ at 330 nW, clearly indicating single-photon emission with sub-Poissonian photon statistics ($g^{(2)}(0) < 0.5$). In this operation mode, however, the $g^{(2)}(0)$ value of our source, i.e. the suppression of multi-photon emission events, is strongly limited by recapture processes^{47,48}. This can be seen from the significant contribution of coincidences close to $\tau = 0$ (cf. inset in Fig. 1 (c)), resulting from the applied above-band excitation scheme. Compared to Ref.⁴² the $g^{(2)}(0)$ value stated here is somewhat higher, which has two possible reasons. Firstly, as we used different fiber-pigtailed QD-devices in both studies, the spectral background contributions to the selected emission line can be different (cf. Fig. 1 (b)). Secondly, and in contrast to Ref.⁴², we did neither apply background subtraction nor fitting, as in the context of quantum communication all detection events

within a given temporal acceptance time window contribute to the key material, independent of whether they originate from a signal photon or an erroneous/background event. Note, that we also have to make this worst-case assumption concerning the photon statistics of our source, when applying temporal filtering to optimize the performance of our testbed (cf. Subsection III B). To improve the single-photon purity for the QKD tests in Section III, we apply resonant p-shell excitation of the QD using the optional external laser resulting in $g^{(2)}(0) = 0.10 \pm 0.01$. Importantly, the function of this external laser can be integrated in the transmitter module by either using more compact lasers with the required performance or even lasers integrated on-chip with the QD-devices. Prospects for higher degrees of laser integration will be discussed in Section IV.

Noteworthy, the dimensions of our benchtop transmitter module $((40 \times 45 \times 13) \text{ cm}^3)$, providing triggered single-photon pulses in a SMF28 fiber, are for the first time competitive with commercial laser-based QKD systems^{49,50}. This is a relative reduction to only 14 % of the O-band QD-SPS's volume reported in Ref.⁴² $((45 \times 60 \times 60) \text{ cm}^3)$.

B. Receiver-Module (Bob)

The receiver module comprises a 4-state polarization decoder with the four output ports connected to the SNSPD-based detection system. Time-tagging electronics (quTAG, qutools GmbH) are used for recording the detection events which are transferred to a personal computer for further processing. Inside the polarization decoder, we realize a passive basis choice using a non-polarizing beamsplitter (BS) with a nominal splitting ratio of 50:50. The discrimination of the polarization after the BS is realized with two Wollaston prisms (WPs) for the detection in the H-V and D-A basis, respectively. The WPs spatially separate two orthogonal polarizations by an angle of 20° with an extinction ratio of up to 1:100,000 and 90 % transmission. For detection in the D-A basis, the respective WP is rotated by an angle of 45° to match the prism's axes with the incoming diagonally or anti-diagonally polarized light. This configuration allows for a low-profile of the overall optical setup. To minimize residual depolarization effects, the rotated WP is implemented in the transmission path of the BS in combination with a quarter wave plate compensating for slight ellipticities introduced by the BS. Note, that although our source is developed for QKD via telecom fibers, we use free-space optics inside the receiver module, due to the achievable lower in-

trinsic QBER and larger spectral bandwidth, both at comparable transmission losses. The polarization decoder is connected to the SNSPDs via four single-mode fibers (type SMF-28). For high coupling efficiencies to these SM fibers, each output port of the decoder features two mirrors for aligning the four beams after the WPs. The overall transmission loss of the polarization decoder η_{Bob} was experimentally determined to -5.2 dB, including the optical losses of -3.0 dB and -2.2 dB due to the SNSPD's finite detection efficiency. The time-tags recorded at the four ports of the receiver module are evaluated using a homemade software package (see Ref.⁵¹ for details).

III. RESULTS

A. Basic QKD Performance Evaluation

The most important performance parameter of a QKD system is the secret key rate. In this work, we are investigating a practical SPS with a finite multi-photon emission probability p_m . The secret key rate for the asymptotic case (i.e. infinite key length) is hence given by^{52,53}

$$S_\infty = S_{\text{sift}} [A(1 - h(e/A)) - f_{\text{EC}}h(e)]. \quad (1)$$

Here, S_{sift} is the sifted key rate, $A = (p_{\text{click}} - p_m)/p_{\text{click}}$ the single-photon detection probability calculated from multi-photon emission probability p_m and overall click probability $p_{\text{click}} \approx \mu \cdot T \cdot \eta_{\text{Bob}} + p_{\text{dc}}$. Here, μ denotes the mean photon number per pulse which Alice couples to the quantum channel, η_{Bob} the efficiency of the receiver module including the detector losses, T is the link transmission, and p_{dc} the dark count probability. The quantum bit error ratio (QBER)⁵⁴ is denoted as e , $h(e)$ the binary Shannon-entropy and f_{EC} is the error correction efficiency. For an ideal SPS (i.e., $p_m = 0$) the factor A equals unity, so A is a correction term for realistic SPSs.

First, we investigate the performance of our Bob module which is characterized by its transmission loss and its contribution to the overall QBER. For this purpose, we sequentially prepared single-photon pulses in horizontal (H), vertical (V), diagonal (D), and antidiagonal (A) polarization and recorded events at all four detection channels of our receiver module. The resulting time-resolved experimental data are summarized in Fig. 2(a) in a

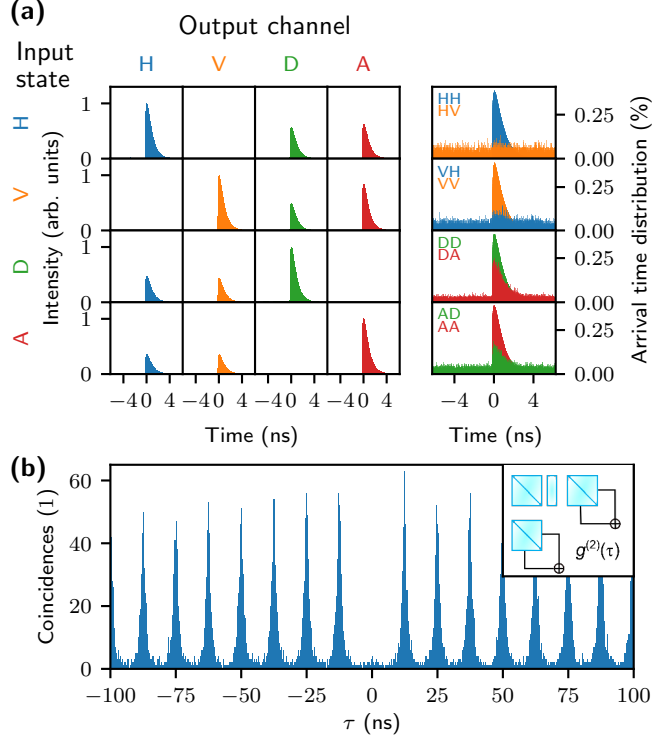


FIG. 2. Characterization of the receiver module Bob using triggered single-photon pulses from Alice as input. (a) Measured photon arrival time distributions at the four detection channels of Bob for single-photon input-polarizations of H, V, D, and A (time-bin width: 1 ps). Measurement data in the left 4x4 matrix are normalized to the maximum of the time-trace of the respective diagonal element. The right panel shows the two data sets for the given input polarization basis for the two respective detection channel of the two bases, and each distribution being normalized to the sum of all events in the respective detection channel (e.g., 'HV' corresponds to the detection channel for V-Polarization measured with input H-polarization.) This photon arrival probability distribution reveals erroneous detection events due to optical imperfections in Bob. (b) Second-order autocorrelation $g^{(2)}(\tau)$ histogram under pulsed resonant p-shell excitation at 1247.9 nm $g^{(2)}(0) = 0.10 \pm 0.01$ (time-bin width: 50 ps, acquisition time: 5 hours). The autocorrelation was obtained by correlating the time-tags recorded at all four detection channels of Bob as shown in the inset.

4x4 matrix, where each row corresponds to the input-polarization and columns to the respective detection channel. Histograms within one row are normalized by the maximum of the time-trace of the respective diagonal element (e.g., all first-row distributions are normalized by the maximum of the HH distribution (blue), while all second-row distributions are

normalized by the maximum of the VV distribution (orange), etc.). The expected behavior of the polarization decoder is clearly observed. For a given input-state, almost all photons are detected in the correct channel of the corresponding basis, i.e., diagonal elements of the matrix, whereas a probabilistic projection is observed in the conjugate basis. Erroneous detection events at the wrong channel are only visible, if the time-resolved measurements are renormalized to the arrival time probability distribution for both output channels in each basis, as depicted in the right panel of Fig. 2 (a). Here, each distribution is normalized to the sum of all events registered in the respective channel (e.g., the HV distribution (orange) is normalized by all clicks registered in the V-channel). In this representation, one can qualitatively distinguish different error contributions. Noise stemming from detector dark counts or stray light results in uncorrelated background noise (cf. HV arrival time distribution (orange)). In our case, the errors due to noise accumulate to a total of (42 ± 1) Hz at the chosen working point of the SNSPDs (mean detection efficiency -2.2 dB). In contrast, optical imperfections inside Bob like finite extinction ratios of polarization optics, result in erroneous events correlated in time with the signal events. These errors are almost negligible in the rectilinear bases but become noticeable in the diagonal basis, e.g., red arrival time distribution in the third row (D-input and A-output). Here, temporarily correlated events are superimposed to the uncorrelated background noise. The discrimination between the two error contributions mentioned above will be exploited in section III.B, to effectively enhance the signal-to-noise-ratio via temporal filtering (cf. Fig. 3). From the experimental data in the right panel of Fig. 2 (a), the contribution to the QBER for a given input polarization can be calculated from the number of erroneous events in the wrong channel divided by the total number of events in the sifted basis, e.g., $\text{QBER}_H = N_V / (N_H + N_V)$. The corresponding QBERs of the respective polarization-channels range between $\text{QBER}_H = 0.35\%$ and $\text{QBER}_D = 0.82\%$. Additional deviations from an ideal setup are due to detection efficiency mismatches between channels (c.f. imbalance between the matrix elements VD and VA in Fig. 2 (a)), which need to be taken into account in full implementation of QKD⁵⁵.

Next, we consider the multi-photon emission probability p_m of our sub-Poissonian quantum light source. This is not as straightforward as in implementations using weak coherent pulses obeying Poissonian statistics. We estimate the upper bound $p_m = \mu^2 g^{(2)}(0)/2$ according to Ref.¹. Note, that finding tighter bounds to p_m could further boost the performance of single-photon QKD in future^{56,57}. In a similar way, recent records in the field of decoy-state

QKD¹⁶ benefited from lower bounds in the finite-key analysis⁵⁸. To determine the photon statistics inside the quantum channel of our QKD testbed, we calculated $g^{(2)}(\tau)$ by correlating all time-tags registered at Bobs’ four output channels as displayed in Fig. 2 (b)⁵¹. Here, recapture processes are strongly suppressed compared to the above-band excitation shown in Fig. 1 (c), due to the resonant p-shell excitation of the quantum emitter. We extract an antibunching value of $g^{(2)}(0) = 0.10 \pm 0.01$ for this measurement by integrating the coincidences over the full repetition period of 12.49 ns. This represents a significant improvement compared to Ref.⁴², where a background-corrected value of $g^{(2)}(0) = 0.15$ was reported for a Stirling-based QD-SPS emitting at O-band wavelengths under above-bandgap excitation. Other fiber-coupled sources achieved similar values ($g^{(2)}(0) = 0.09$)⁵⁹, but at lower temperatures using liquid helium infrastructure. Limiting factors to the $g^{(2)}(0)$ observed in our work are related to a finite suppression and internal reflections of the laser emission as well as residual background contributions from other QD emission lines (cf. Fig. 1 (c)). Applying temporal filtering as a post-process to the recorded timestamps, we estimate the contribution of scattered laser photons and events due to QD re-excitation to the overall signal to 2.5%. Removing these events results in a reduction of $g^{(2)}(0)$ from 0.10 to 0.06, with the remaining imperfection attributed to the residual background emission of nearby QD emission lines. The finite laser suppression in our experiment is mainly caused by reflections and scattering events associated with the FC/PC connectors in combination with a finite transmission of the bandpassfilter at the laser wavelength in our all-fiber-coupled measurement configuration. Straightforward improvements include the use of FC/APC connectors, a bandpassfilter with better side-band suppression ratios, and the use of coherent excitation schemes and/or QD-devices with improved spectral purity. With these improvements, our all-fiber bench-top device is anticipated to become competitive or even surpassing state-of-the-art values of $g^{(2)}(0) = 0.027$ ⁶⁰ (at 10 K) and $g^{(2)}(0) = 0.026$ ⁶¹ (at 40 K) for deterministically and non-deterministically fabricated O-band QD-devices, respectively, obtained in experiments using standard bulky cryotechnology, high-NA microscope objectives, and using grating spectrometers for spectral filtering. Not least, the $g^{(2)}(\tau)$ in the present work indicates a blinking behavior⁶² which can be described by the “on-off” model from Ref.⁶³. The respective time constants are $\tau_{\text{on}} = (482.3 \pm 2.5)$ ns and $\tau_{\text{off}} = (275.1 \pm 1.0)$ ns yielding a QD “on”-state efficiency of 57% reducing the efficiency of our source (see also Supplementary Material, Figure S1). This blinking effect is not a fundamental limit and can possibly be overcome

by optimizing the QD growth or embedding QDs in charge tunable devices⁶⁴. In addition, we observe a higher photon detection rate, i.e., raw key rate, of (4.72 ± 0.13) kHz compared to 1.15 kHz in Ref.⁴² due to reduced losses in the detection apparatus. From the raw key rate of $S_{\text{raw}} = (4.72 \pm 0.13)$ kHz, the transmission of the Bob module $\eta_{\text{Bob}} = 0.3$, and the clock rate $f = 80$ MHz, we determine the mean photon number per pulse into the quantum channel via $\mu = S_{\text{raw}}\eta_{\text{Bob}}^{-1}f^{-1} = 0.0002$. We note here that employing our source in a full implementation would yield a slightly lower μ due to the use of an electro-optical modulator with typical internal losses of about -2 dB.

B. Optimization via temporal filtering

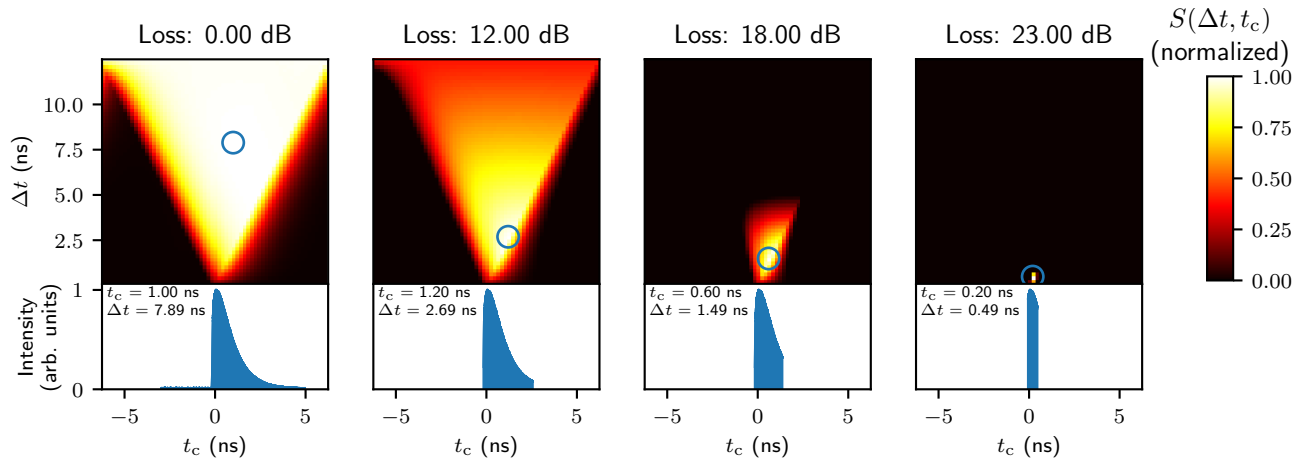


FIG. 3. 2D temporal filtering for optimization of the secret key rate. For the optimization, a subset of the measurement in Figure 2(b) was used for reasonable computing times. Expected secret key rate fraction $S(\Delta t, t_c)$ from Eq. (1) as a function of the temporal width Δt and the center t_c of the acceptance time window. $S(\Delta t, t_c)$ is normalized to the maximum achievable secret key rate for each map individually. For the analysis the QBER and the sifted key fraction were considered in a two-dimensional parameter space $(\Delta t, t_c)$, while $g^{(2)}(0)$ was fixed to its unfiltered value (cf. discussion in main text). From the parameters at 0 dB transmission losses, three different loss scenarios (12 dB, 18 dB, 23 dB) are simulated. A blue circle marks the optimal parameter sets resulting in a maximal secure key rate. Additionally, the evaluated optimal acceptance time window is depicted in the time-resolved measurements in the lower panels.

Based on the parameter analysis from our QKD testbed, the secret key rate expected

in a full implementation of QKD can be estimated. In this section, we evaluate optimal performance regimes by applying a routine for 2D temporal filtering recently reported by our group in Ref.⁵¹. As the quantum emitter has a relatively short lifetime (0.9 ns) compared to the pulse repetition period (12.49 ns), we can efficiently reduce the contribution of clicks due to detector noise by reducing the temporal acceptance window. This results in a reduction of the QBER - ideally down to the limit of below 0.4% caused by optical imperfections in the worst channel. On the other hand, the applied temporal filter will also reduce the number of bits available for key distillation. Choosing the optimal trade-off between QBER and sifted key material, the secure key can be maximized for a given channel loss (see Supplementary Material, Figure S2 for details). Due to the asymmetric shape of the photon arrival time distribution, it is beneficial to vary both the center t_c and the width Δt of the acceptance time window. Important with respect to the protocol security is, that although we use temporal filtering in the following to maximize the secret key rate, we always make the worst-case assumption concerning the photon statistics of our source by using the full unfiltered $g^{(2)}(0)$ value. While in principle an additional performance gain is achievable by exploiting the temporally filtered $g^{(2)}(0)$, this would open security loopholes without additional extensions to the protocol implementation (see Ref.⁵¹ for details). Figure 3 depicts the estimated asymptotic secret key rate $S(\Delta t, t_c)$ calculated according to Eq. (1) in heat-maps for different loss regimes together with the resulting optimal temporal acceptance window (cf. lower panels and circle in heat-maps) resulting in the largest possible secret key rate. We used our experimental parameters $g^{(2)}(0)$ and μ as stated above. The dark count probability p_{dc} scales linearly with the acceptance time window. In contrast, the reduced click rate cannot be modelled so easily due to the distribution of the arrival time probabilities. The fraction of the signal resulting in different values of p_{click} was therefore evaluated for each acceptance time window individually (c.f. Ref.⁵¹, Supplementary Note 3) by rejecting detection events outside the temporal filter. As Eq. (1) is a function of the link loss T , we can simulate the expected key rate for different loss regimes and still apply the temporal filtering. Accounting for the temporal resolution of our experimental setup (convolution of the detector response and the time-tagging device) we used a lower limit for the acceptance time window of 90 ps. Already for a back-to-back transmission (i.e. zero channel loss) discarding some of the sifted key can lead to higher $S(\Delta t, t_c)$ due to the improved signal-to-noise ratio. But not only does the 2D optimization increase $S(\Delta t, t_c)$, it

allows also to extend the achievable transmission distance. This is exemplarily depicted in the 18 dB and 23 dB case in Fig. (3). Black regions indicate acceptance time windows for which no secret key can be exchanged. In those higher loss regimes, without applying any temporal filtering, no secret key could be exchanged. Thus, this optimization results in an effective range extension.

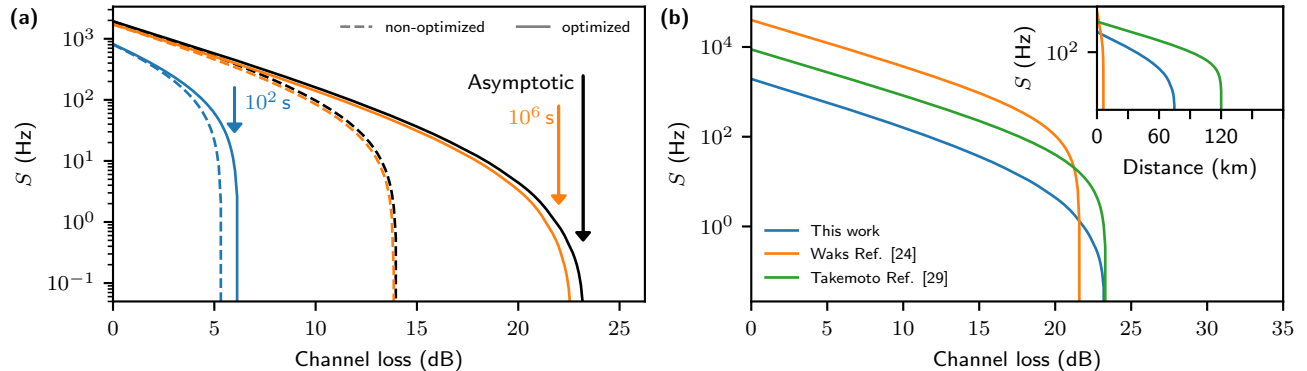


FIG. 4. Rate-loss diagrams considering our experimental data from Fig. 3. (a) Comparison between asymptotic (Eq. (1)) and finite (Eq. (2)) key rate. The secret key rate S in full QKD- implementations is calculated from our experimental parameters. The values without optimizations are depicted with dashed lines, the optimized values with solid lines, respectively. (b) Comparison of our optimized parameter set with previous QD-based QKD implementations for fiber channel. We assume 0.31 dB/km for our source at 1321 nm, for Ref.²⁹ 0.194 dB/km at 1580.5 nm, and for Ref.²⁴ 3.5 dB/km at 877 nm.

In practical scenarios it is not sufficient to consider only the asymptotic case, as the limited transmission time or transferred data size limits not only the achievable rate at a given distance but also the achievable distance itself. This becomes particular relevant for QKD in free-space optical systems with a relative movement between transmitters and receivers (e.g. airplanes⁶⁵, satellites^{66–68}), at which stable link-conditions cannot be maintained for a long time. The loss budget of fiber-based connections needs to include finite key size effects especially in regimes with high losses and therefore long transmission times. Adapting the finite size key corrections of Ref.⁶⁹ the key rate in Eq. (1) is modified:

$$S_{\text{finite}}(N) = nA(1 - h(\bar{e}/A)) - nf_{\text{ECH}}(e) - \Delta(n). \quad (2)$$

First, one has to take into account that not all of the sifted key S_{sift} can be used for the secret key but a fraction of it has to be discarded for parameter estimation. Out of the sifted

TABLE I. Relevant parameters to calculate the secret key rates in Fig.4 (b). The parameters for Ref.²⁴ and Ref.²⁹ are based on the respective published experimental data. The efficiency η_{Bob} and p_{dc} are lower when applying individual filtering.

	Ref. ²⁴	Ref. ²⁹	This Work
λ (nm)	877	1580.5	1321
μ	0.007	0.009	0.0002
p_{dc}	$10.5 \cdot 10^{-7}$	$3 \cdot 10^{-7}$	$5.25 \cdot 10^{-7}$
e_{detector}	0.025	0.023	0.010
η_{Bob}	0.24	0.048	0.3
$g^{(2)}(0)$	0.14	0.0051	0.10

events a number of m is taken for parameter estimation and the remaining n bits are used for the key generation. Taking only a finite sample m might lead to deviations between the estimated and the actual error rate. This is taken into consideration by

$$\tilde{e} = e + \sqrt{(\ln(1/\epsilon_{\text{PE}}) + 2 \ln(m+1))/2m} \quad (3)$$

where ϵ_{PE} is the probability for such deviations to occur. Additional finite corrections are subsumed as $\Delta(n)$

$$\Delta(n) = 7n \sqrt{\frac{1}{n} \log_2 \frac{2}{\tilde{\epsilon}}} + 2 \log_2 \frac{1}{\epsilon_{\text{PA}}} + \log_2 \frac{2}{\epsilon_{\text{EC}}}, \quad (4)$$

with the overall security parameter $\epsilon = \epsilon_{\text{EC}} + \tilde{e} + \epsilon_{\text{PE}} + \epsilon_{\text{PA}}$ including the failure probabilities for the error correction ϵ_{EC} , the entropy estimation $\tilde{\epsilon}$, the parameter estimation ϵ_{PE} , and the privacy amplification ϵ_{PA} ⁶⁹.

The rate-loss diagram in Fig. 4 (a) comparatively illustrates the asymptotic and finite-size secret key rates S calculated via Eq. (1) and Eq. (2), respectively, considering our experimentally determined parameters. Additionally, we consider each case with and without applying optimized 2D temporal filters. To this end we maximize S for each loss individually, by choosing optimal parameter sets as exemplary depicted in Fig. 3 (see Supplementary Material, Fig. S3 for the optimized parameter sets). This contrasts with Ref.⁵¹, where we evaluated rate-loss dependencies for exemplary settings of the acceptance window. For a qualitative understanding, each curve can be divided into two regimes: the absorption limited regime at small channel loss and the noise limited regime at large channel loss. At

small channel loss, S follows a linear trend (in logarithmic scaling) due to the absorption in the quantum channel. In the regime of larger losses, this trend changes to a multi-exponential drop of S once the probability to register an event due to detector dark counts becomes comparable to the probability to detect a signal photon ($p_{\text{dc}} \approx p_{\text{signal}}$). Quantitatively, we extract a maximal tolerable loss for our test-system of 13.96 dB in the non optimized asymptotic case. However, with 2D temporal filtering individually optimized for each loss, one does not only get a slightly higher secret key rate back-to-back but can additionally extend the tolerable losses up to 23.19 dB. In a state-of-the-art single-mode fiber with losses of 0.31 dB/km at 1300 nm this corresponds to a range extension of almost 30 km from 45.0 km to 74.8 km. Taking finite key size effects into account Alice has to send for a minimum transmission time of 18 seconds to yield a positive S in the back-to-back case. Increasing the transmission time by one order of magnitude to 100 seconds would already allow for 6.8 dB of loss in the optimized case. With unpractical transmission times of 1×10^6 seconds one could almost reach the asymptotic case. By comparing the two cases of rather short and long transmission times, one can see that the range extension gained by applying 2D temporal filtering increases with the transmission time. The implementation and discussion of finite-size effects presented above is an important step towards practical implementations of single-photon QKD, also compared to our previous work in Ref.⁵¹ discussing key rates only in the asymptotic limit.

C. Comparison and Discussion

Finally, we compare the extrapolated performance of our testbed with selected previous implementations of QKD. As mentioned already in the introduction, several QKD-experiments using QD-sources have been reported (as summarized in Ref.³³). For our comparison, we select the QKD experiments reported in Ref.²⁴ and Ref.²⁹ employing QD-based SPSs operating at 877 nm and 1580.5 nm, respectively. This choice was made to cover, together with our source, the technically most relevant wavelength ranges (1st, 2nd, and 3rd telecom window) for fiber-based applications and due to the high secure key rates achieved in these experiments. We assume implementations in SM fiber with losses of 0.31 dB/km in case of our work, 0.194 dB/km for Ref.²⁹, and 3.5 dB/km for Ref.²⁴, corresponding to the typical losses in optical fibers at the implementation's specified wavelengths. For the sake of

comparison we calculated the key rates for the asymptotic case, representing the ultimate limit for each system. The parameters used for the comparison are summarized in Tab. I. Figure 4 (b) displays the resulting curves in a rate-loss diagram and the corresponding rate-distance diagram as inset. While the first proof-of-principle implementation by Waks et al. in 2002 achieved a higher $\mu = 0.007$ compared to our present stand-alone device, their wavelength is not ideal for fiber based implementations. Therefore, the achievable distance in optical fiber is strongly limited (cf. Figure 4 (b), inset), although their implementation reaches a maximal tolerable loss of 21.6 dB. Among the three QKD experiments, our optimized case achieves the highest tolerable loss of 23.19 dB, due to low dark count levels and low intrinsic QBERs caused by our receiver module. One should note, that the latter will increase slightly for a full implementations using our SPS, due to additional contributions to the QBER caused by dynamic state preparation via EOMs. To date, the QKD system reported by Takemoto et al. in Ref.²⁹ achieves the highest possible transmission distance exceeding 100 km, due to the low fiber-loss at C-band wavelengths. Please note, that deviations in the achievable transmission distance compared to the original references are related to the use of slightly different rate equations or p_m and a different f_{EC} . Not least, also the previous implementations cited here might benefit from 2D temporal filtering, which could allow for performance improvements. While the efficiency of our all-fiber-coupled benchtop SPS is so far not compatible with the state-of-the-art in terms of μ inside the quantum channel, we anticipate substantially enhanced performance in the future employing the improvements discussed in the conclusion below.

In terms of practicability and compactness, our QKD testbed, with a size of the transmitter comparable to commercial laser-based QKD systems, represents a milestone compared to previous QKD experiments using sub-Poissonian quantum light sources. In terms of the performance, our source and any sub-Poissonian QKD experiment reported to date is not yet competitive with WCP-based implementations. The current record for direct point-to-point QKD at C-band wavelength reported by Boaron et al.¹⁶ achieved a tolerable loss of 71.9 dB corresponding to a communication distance of 421 km in ultra-low loss optical fiber. For single-photon QKD, significant improvements are required in both, the efficiency μ and $g^{(2)}(0)$ to become competitive or even surpass WCP-based implementations. In WCP-based implementations obeying Poisson statistics, there is a fundamental upper limit of $\mu = 0.37$ (cf. Ref.⁵¹ for details). For deterministic single-photon sources, μ is in principle only limited

by technological challenges, e.g., photon-collection and fiber-coupling efficiencies. Recently a QD-SPS with an SM fiber-coupled efficiency of 57% and $g^{(2)}(0) = 0.021$ was reported at a wavelength of 919 nm¹⁰ and the authors claimed 80% efficiency within reach. Still, overcoming the limit of 37% inside the quantum channel, including losses for qubit-state preparation, is a challenge in practical implementation. While the efficiency of a SPS is important in the regime of low channel losses, low multi-photon probabilities p_m become the limiting factor at high channel losses²⁴. Therefore, it is important to improve $g^{(2)}(0)$ as far as possible without reducing the efficiency μ . In contrast to sources based on spontaneous parametric down conversion, no fundamental trade-off between low $g^{(2)}(0)$ values and high efficiencies exists for QD sources. Therefore, further improvements in device technology will enable to simultaneously achieve record low $g^{(2)}(0)$ values (c.f. $g^{(2)}(0) = (7.5 \pm 1.6) \times 10^{-5}$ in Ref.⁷) and record efficiencies in future QD devices. In addition, as mentioned in section III.A, finding tighter bounds for estimating p_m can result in a boost of the performance of sub-Poissonian QKD. Important to note, is that the discussion above refers to point-to-point QKD in a prepare-and-measure configuration. In recent entanglement-based QKD experiments using QD-based sources, it was shown that already much lower efficiencies than 0.37 are sufficient to beat QKD implementations based on spontaneous parametric down conversion (cf. Ref.³², Supplemental Material).

IV. SUMMARY & CONCLUSIONS

We demonstrated the first test experiments evaluating a compact and plug&play bench-top solid state based SPS for applications in QKD. For this purpose, we developed the most compact QD-SPS operating in the telecom O-band reported to date. The source module housed in a 19 inch rack unit comprises a fiber-pigtailed QD integrated into a Stirling cryocooler, and a fiber-based band-pass filter. On receiver side of the QKD testbed, we employed a 4-state polarization decoder optimized for O-band wavelengths allowing for low intrinsic QBER. Using this testbed, we demonstrated that maximal tolerable losses of 23.19 dB are achievable in full implementations with this system, if optimization routines are applied for a 2D temporal acceptance time window. We further investigated the impact of finite key size effects to the performance of our testbed and compared our results with previous implementations of QKD using QD-SPSs.

The benchtop transmitter module developed in this work, with a size competitive to commercial laser-based QKD systems, represents a milestone compared to previous QD-based QKD experiments in terms of compactness and practicability, while offering a comparable performance level. In terms of efficiency and multi-photon emission probability, the performance is not yet sufficient to compete with state-of-the-art decoy-state QKD systems using WCPs. To boost the performance of sub-Poissonian QKD in the future, advanced fiber-coupled SPSs based on circular Bragg grating (CBG) cavities can be employed, which show prospects for photon collection efficiencies exceeding 80% in SM fiber-pigtailed configuration⁷⁰. Moreover, exploiting microcavities with slight ellipticities, highly polarized SPSs can be realized⁹ to further reduce the losses inside the sender module. Another route for improvements concerns the implementation of GHz clock rates, e.g., by using electrically driven cavity-enhanced QD-SPSs¹¹, which can be directly fiber-pigtailed using a technique recently developed in our group³⁹. Possible future improvements concern the integration of lasers in the transmitter module, which are suitable for the coherent excitation of quantum emitters. Two routes appear promising in this context. The first option is the use of more compact pulsed lasers suitable for the coherent excitation of quantum emitters, which can be achieved by combining spectrally tunable continuous-wave lasers with intensity modulators⁷¹. Here, also spectrally tunable fiber-coupled QD-devices³⁸ are interesting and provide an additional tuning knob. The second option, offering the highest degree of device integration, is the use of lasers integrated on-chip nearby the quantum-light emitting device itself^{72,73} - a concept that was previously tested in installed fiber networks⁷⁴. Not least, lower operating temperatures could be achieved by advances in the development of compact cryocoolers, enabling the generation of photons with high indistinguishability⁷⁵, paving the way for implementations of quantum communication beyond direct point-to-point links^{76,77} using benchtop deterministic quantum light sources. Although this work focused on direct point-to-point QKD, the progress achieved, and prospects discussed in this work are important for practical implementations of advanced schemes of quantum information, e.g., quantum repeaters², where quantum advantages against classical light states get even more apparent.

SUPPLEMENTARY MATERIAL

See the supplementary material in section for additional experimental data on the blinking behavior (Fig. S1) and the effect of temporal filtering on the signal fraction and QBER as recorded for all four detection channels (Fig. S2). In addition, we provide the optimal parameter sets for each individual temporal acceptance window applied for optimizing the rate-loss dependencies in Fig. 4 (a) (Fig. S3).

ACKNOWLEDGMENTS

We gratefully acknowledge financial support by the German Federal Ministry of Education and Research (BMBF) via project “QuSecure” (Grant No. 13N14876) within the funding program Photonic Research Germany and by the Einstein Foundation via the Einstein Research Unit “Quantum Devices”. The development of the QD-SPS has further been supported by the project “FI-SEQUUR” jointly financed by the European Regional Development Fund (EFRE) of the European Union in the framework of the programme to promote research, innovation, and technologies (Pro FIT) in Germany, and the National Centre for Research and Development in Poland within the 2nd Poland-Berlin Photonics Programme (Grant No. 2/POLBER-2/2016)). S. Rodt and S. Reitzenstein further acknowledge support by the German Science Foundation (DFG) via CRC 787 and S. Burger support by the BMBF via project “MODAL/NanoLab” (Grant No.: 05M20ZBM). Not least, support by the Polish National Agency for Academic Exchange is gratefully acknowledged.

AUTHOR DECLARATIONS

Author contributions

TK designed and set up the QKD testbed with support by FU, ran the experiments together with LR, and evaluated the experimental data. LR assembled parts of the stand-alone single-photon source, integrated the fiber-pigtailed QD, and operated the source. JG, NS, and S Rodt grew and processed the QD sample under supervision of S Reitzenstein who conceived the QD-SPS development and fabrication. AM and KZ fiber-pigtailed the QD under supervision of WU and GS using the high-NA specialty fiber developed by PM

and KD. KD connected the specialty and the standard SM-fiber. SB contributed numerically optimized devices designs for processing the QD sample. TK, LR, and TH wrote the manuscript with input from all authors. TK and LR contributed equally to this work. TH conceived the experiments presented in this work and supervised all efforts on the QKD testbed.

Conflict of interest

The authors have no conflicts to disclose.

REFERENCES

- ¹E. Waks, C. Santori, and Y. Yamamoto, “Security aspects of quantum key distribution with sub-poisson light,” [Physical Review A](#) **66**, 042315 (2002).
- ²H.-J. Briegel, W. Dür, J. I. Cirac, and P. Zoller, “Quantum repeaters: The role of imperfect local operations in quantum communication,” [Physical Review Letters](#) **81**, 5932–5935 (1998).
- ³I. Aharonovich, D. Englund, and M. Toth, “Solid-state single-photon emitters,” [Nature Photonics](#) **10**, 631–641 (2016).
- ⁴Y. Arakawa and M. J. Holmes, “Progress in quantum-dot single photon sources for quantum information technologies: A broad spectrum overview,” [Applied Physics Reviews](#) **7**, 021309 (2020).
- ⁵G. Zhang, Y. Cheng, J.-P. Chou, and A. Gali, “Material platforms for defect qubits and single-photon emitters,” [Applied Physics Reviews](#) **7**, 031308 (2020).
- ⁶T. Miyazawa, K. Takemoto, Y. Nambu, S. Miki, T. Yamashita, H. Terai, M. Fujiwara, M. Sasaki, Y. Sakuma, M. Takatsu, T. Yamamoto, and Y. Arakawa, “Single-photon emission at 1.5 micrometer from an InAs/InP quantum dot with highly suppressed multiphoton emission probabilities,” [Applied Physics Letters](#) **109**, 132106 (2016).
- ⁷L. Schweickert, K. D. Jöns, K. D. Zeuner, S. F. C. da Silva, H. Huang, T. Lettner, M. Reindl, J. Zichi, R. Trotta, A. Rastelli, and V. Zwiller, “On-demand generation of background-free single photons from a solid-state source,” [Applied Physics Letters](#) **112**, 093106 (2018).

- ⁸J. Liu, R. Su, Y. Wei, B. Yao, S. F. C. da Silva, Y. Yu, J. Iles-Smith, K. Srinivasan, A. Rastelli, J. Li, and X. Wang, “A solid-state source of strongly entangled photon pairs with high brightness and indistinguishability,” *Nature Nanotechnology* **14**, 586–593 (2019).
- ⁹H. Wang, H. Hu, T.-H. Chung, J. Qin, X. Yang, J.-P. Li, R.-Z. Liu, H.-S. Zhong, Y.-M. He, X. Ding, Y.-H. Deng, Q. Dai, Y.-H. Huo, S. Höfling, C.-Y. Lu, and J.-W. Pan, “On-demand semiconductor source of entangled photons which simultaneously has high fidelity, efficiency, and indistinguishability,” *Physical Review Letters* **122** (2019).
- ¹⁰N. Tomm, A. Javadi, N. O. Antoniadis, D. Najer, M. C. Löbl, A. R. Korsch, R. Schott, S. R. Valentin, A. D. Wieck, A. Ludwig, and R. J. Warburton, “A bright and fast source of coherent single photons,” *Nature Nanotechnology* **16**, 399–403 (2021).
- ¹¹A. Schlehahn, A. Thoma, P. Munnely, M. Kamp, S. Höfling, T. Heindel, C. Schneider, and S. Reitzenstein, “An electrically driven cavity-enhanced source of indistinguishable photons with 61% overall efficiency,” *APL Photonics* **1** (2016).
- ¹²G. Shooter, Z.-H. Xiang, J. R. A. Müller, J. Skiba-Szymanska, J. Huwer, J. Griffiths, T. Mitchell, M. Anderson, T. Müller, A. B. Krysa, R. M. Stevenson, J. Heffernan, D. A. Ritchie, and A. J. Shields, “1GHz clocked distribution of electrically generated entangled photon pairs,” *Optics Express* **28**, 36838 (2020).
- ¹³C. H. Bennett, F. Bessette, G. Brassard, L. Salvail, and J. Smolin, “Experimental quantum cryptography,” *Journal of Cryptology* **5**, 3–28 (1992).
- ¹⁴X.-B. Wang, “Beating the photon-number-splitting attack in practical quantum cryptography,” *Physical Review Letters* **94**, 230503 (2005).
- ¹⁵H.-K. Lo, X. Ma, and K. Chen, “Decoy state quantum key distribution,” *Physical Review Letters* **94**, 230504 (2005).
- ¹⁶A. Boaron, G. Boso, D. Rusca, C. Vulliez, C. Autebert, M. Caloz, M. Perrenoud, G. Gras, F. Bussi eres, M.-J. Li, D. Nolan, A. Martin, and H. Zbinden, “Secure quantum key distribution over 421 km of optical fiber,” *Phys. Rev. Lett.* **121**, 190502 (2018).
- ¹⁷A. Badolato, K. Hennessy, M. Atat ure, J. Dreiser, E. Hu, P. M. Petroff, and A. Imamog lu, “Deterministic coupling of single quantum dots to single nanocavity modes,” *Science* **308**, 1158–1161 (2005).
- ¹⁸A. Dousse, L. Lanco, J. Suffczyński, E. Semenova, A. Miard, A. Lemaître, I. Sagnes, C. Roblin, J. Bloch, and P. Senellart, “Controlled light-matter coupling for a single quantum dot embedded in a pillar microcavity using far-field optical lithography,” *Physical*

- [Review Letters](#). **101**, 267404 (2008).
- ¹⁹M. Gschrey, F. Gericke, A. Schüßler, R. Schmidt, J.-H. Schulze, T. Heindel, S. Rodt, A. Strittmatter, and S. Reitzenstein, “In situ electron-beam lithography of deterministic single-quantum-dot mesa-structures using low-temperature cathodoluminescence spectroscopy,” [Applied Physics Letters](#) **102**, 251113 (2013).
- ²⁰M. Gschrey, A. Thoma, P. Schnauber, M. Seifried, R. Schmidt, B. Wohlfeil, L. Krüger, J. H. Schulze, T. Heindel, S. Burger, F. Schmidt, A. Strittmatter, S. Rodt, and S. Reitzenstein, “Highly indistinguishable photons from deterministic quantum-dot microlenses utilizing three-dimensional in situ electron-beam lithography,” [Nature Communications](#) **6**, 7662 (2015).
- ²¹N. Somaschi, V. Giesz, L. De Santis, J. C. Loredó, M. P. Almeida, G. Hornecker, S. L. Portalupi, T. Grange, C. Antón, J. Demory, C. Gómez, I. Sagnes, N. D. Lanzillotti-Kimura, A. Lemaître, A. Auffeves, A. G. White, L. Lanco, and P. Senellart, “Near-optimal single-photon sources in the solid state,” [Nat. Photon.](#) **10**, 340–345 (2016).
- ²²T. Heindel, A. Thoma, M. von Helversen, M. Schmidt, A. Schlehahn, M. Gschrey, P. Schnauber, J. H. Schulze, A. Strittmatter, J. Beyer, S. Rodt, A. Carmele, A. Knorr, and S. Reitzenstein, “A bright triggered twin-photon source in the solid state,” [Nature Communications](#) **8**, 14870 (2017).
- ²³S. Rodt, S. Reitzenstein, and T. Heindel, “Deterministically fabricated solid-state quantum-light sources,” [Journal of Physics: Condensed Matter](#) **32**, 153003 (2020).
- ²⁴E. Waks, K. Inoue, C. Santori, D. Fattal, J. Vuckovic, G. S. Solomon, and Y. Yamamoto, “Secure communication: Quantum cryptography with a photon turnstile,” [Nature](#) **420**, 762 (2002).
- ²⁵P. M. Intallura, M. B. Ward, O. Z. Karimov, Z. L. Yuan, P. See, P. Atkinson, D. A. Ritchie, and A. J. Shields, “Quantum communication using single photons from a semiconductor quantum dot emitting at a telecommunication wavelength,” [Journal of Optics A: Pure and Applied Optics](#) **11**, 054005 (2009).
- ²⁶R. J. Collins, P. J. Clarke, V. Fernández, K. J. Gordon, M. N. Makhonin, J. A. Timpson, A. Tahraoui, M. Hopkinson, A. M. Fox, M. S. Skolnick, and G. S. Buller, “Quantum key distribution system in standard telecommunications fiber using a short wavelength single photon source,” [Journal of Applied Physics](#) **107**, 073102 (2010).

- ²⁷T. Heindel, C. A. Kessler, M. Rau, C. Schneider, M. Fürst, F. Hargart, W.-M. Schulz, M. Eichfelder, R. Roßbach, S. Nauerth, M. Lermer, H. Weier, M. Jetter, M. Kamp, S. Reitzenstein, S. Höfling, P. Michler, H. Weinfurter, and A. Forchel, “Quantum key distribution using quantum dot single-photon emitting diodes in the red and near infrared spectral range,” *New Journal of Physics* **14**, 083001 (2012).
- ²⁸M. Rau, T. Heindel, S. Unsleber, T. Braun, J. Fischer, S. Frick, S. Nauerth, C. Schneider, G. Vest, S. Reitzenstein, M. Kamp, A. Forchel, S. Höfling, and H. Weinfurter, “Free space quantum key distribution over 500 meters using electrically driven quantum dot single-photon sources—a proof of principle experiment,” *New Journal of Physics* **16**, 043003 (2014).
- ²⁹K. Takemoto, Y. Nambu, T. Miyazawa, Y. Sakuma, T. Yamamoto, S. Yorozu, and Y. Arakawa, “Quantum key distribution over 120 km using ultrahigh purity single-photon source and superconducting single-photon detectors,” *Scientific Reports* **5**, 14383 (2015).
- ³⁰B. Dzurnak, R. M. Stevenson, J. Nilsson, J. F. Dynes, Z. L. Yuan, J. Skiba-Szymanska, I. Farrer, D. A. Ritchie, and A. J. Shields, “Quantum key distribution with an entangled light emitting diode,” *Applied Physics Letters* **107**, 261101 (2015).
- ³¹F. B. Basset, M. Valeri, E. Roccia, V. Muredda, D. Poderini, J. Neuwirth, N. Spagnolo, M. B. Rota, G. Carvacho, F. Sciarrino, and R. Trotta, “Quantum key distribution with entangled photons generated on demand by a quantum dot,” *Science Advances* **7**, eabe6379 (2021).
- ³²C. Schimpf, M. Reindl, D. Huber, B. Lehner, S. F. C. D. Silva, S. Manna, M. Vyvlecka, P. Walther, and A. Rastelli, “Quantum cryptography with highly entangled photons from semiconductor quantum dots,” *Science Advances* **7**, eabe8905 (2021).
- ³³D. A. Vajner, L. Rickert, T. Gao, K. Kaymazlar, and T. Heindel, “Quantum communication using semiconductor quantum dots,” arXiv2108.13877 (2021).
- ³⁴C. H. Bennett and G. Brassard, “Quantum cryptography: Public key distribution and coin tossing,” Proceedings of IEEE International Conference on Computers, Systems and Signal Processing, Bangalore, India , 175–179 (1984).
- ³⁵V. Scarani, H. Bechmann-Pasquinucci, N. J. Cerf, M. Dušek, N. Lütkenhaus, and M. Peev, “The security of practical quantum key distribution,” *Reviews of Modern Physics* **81**, 1301–1350 (2009).

- ³⁶X. Xu, I. Toft, R. T. Phillips, J. Mar, K. Hammura, and D. A. Williams, “‘plug and play’ single-photon sources,” [Applied Physics Letters](#) **90**, 061103 (2007).
- ³⁷D. Cadeddu, J. Teissier, F. R. Braakman, N. Gregersen, P. Stepanov, J.-M. Gérard, J. Claudon, R. J. Warburton, M. Poggio, and M. Munsch, “A fiber-coupled quantum-dot on a photonic tip,” [Applied Physics Letters](#) **108**, 011112 (2016).
- ³⁸H. Snijders, J. Frey, J. Norman, V. Post, A. Gossard, J. Bowers, M. van Exter, W. Löffler, and D. Bouwmeester, “Fiber-coupled cavity-QED source of identical single photons,” [Physical Review Applied](#) **9**, 031002 (2018).
- ³⁹L. Rickert, F. Schröder, T. Gao, C. Schneider, S. Höfling, and T. Heindel, “Fiber-pigtailing quantum-dot cavity-enhanced light emitting diodes,” [Applied Physics Letters](#) **119**, 131104 (2021).
- ⁴⁰A. Schlehahn, L. Krüger, M. Gschrey, J.-H. Schulze, S. Rodt, A. Strittmatter, T. Heindel, and S. Reitzenstein, “Operating single quantum emitters with a compact stirling cryocooler,” [Review of Scientific Instruments](#) **86**, 013113 (2015).
- ⁴¹A. Schlehahn, S. Fischbach, R. Schmidt, A. Kaganskiy, A. Strittmatter, S. Rodt, T. Heindel, and S. Reitzenstein, “A stand-alone fiber-coupled single-photon source,” [Scientific Reports](#) **8**, 1340 (2018).
- ⁴²A. Musiał, K. Żołnaczyk, N. Srocka, O. Kravets, J. Große, J. Olszewski, K. Poturaj, G. Wójcik, P. Mergo, K. Dybka, M. Dyrkacz, M. Dłubek, K. Lauritsen, A. Bültner, P.-I. Schneider, L. Zschiedrich, S. Burger, S. Rodt, W. Urbanńczyk, G. Sęk, and S. Reitzenstein, “Plug&play fiber-coupled 73 kHz single-photon source operating in the telecom o-band,” [Advanced Quantum Technologies](#) **3**, 2000018 (2020).
- ⁴³F. Guffarth, R. Heitz, A. Schliwa, O. Stier, N. N. Ledentsov, A. R. Kovsh, V. M. Ustinov, and D. Bimberg, “Strain engineering of self-organized inas quantum dots,” [Phys. Rev. B](#) **64**, 085305 (2001).
- ⁴⁴K. Żołnaczyk, A. Musiał, N. Srocka, J. Große, M. J. Schlösinger, P.-I. Schneider, O. Kravets, M. Mikulicz, J. Olszewski, K. Poturaj, G. Wójcik, P. Mergo, K. Dybka, M. Dyrkacz, M. Dłubek, S. Rodt, S. Burger, L. Zschiedrich, G. Sęk, S. Reitzenstein, and W. Urbanńczyk, “Method for direct coupling of a semiconductor quantum dot to an optical fiber for single-photon source applications,” [Optics Express](#) **27**, 26772 (2019).
- ⁴⁵P.-I. Schneider, N. Srocka, S. Rodt, L. Zschiedrich, S. Reitzenstein, and S. Burger, “Numerical optimization of the extraction efficiency of a quantum-dot based single-photon

- emitter into a single-mode fiber,” [Optics Express](#) **26**, 8479–8492 (2018).
- ⁴⁶P.-I. Schneider, X. Garcia Santiago, V. Soltwisch, M. Hammerschmidt, S. Burger, and C. Rockstuhl, “Benchmarking five global optimization approaches for nano-optical shape optimization and parameter reconstruction,” [ACS Photonics](#) **6**, 2726–2733 (2019).
- ⁴⁷T. Aichele, V. Zwiller, and O. Benson, “Visible single-photon generation from semiconductor quantum dots,” [New Journal of Physics](#) **6**, 90 (2004).
- ⁴⁸P. A. Dalgarno, J. McFarlane, D. Brunner, R. W. Lambert, B. D. Gerardot, R. J. Warburton, K. Karrai, A. Badolato, and P. M. Petroff, “Hole recapture limited single photon generation from a single n-type charge-tunable quantum dot,” [Applied Physics Letters](#) **92**, 193103 (2008).
- ⁴⁹D. Stucki, N. Gisin, O. Guinnard, G. Ribordy, and H. Zbinden, “Quantum key distribution over 67 km with a plug&play system,” [New Journal of Physics](#) **4**, 41–41 (2002).
- ⁵⁰For companies see e.g., ID Quantique SA, Toshiba Europe Limited, MagiQ Technologies.
- ⁵¹T. Kupko, M. von Helversen, L. Rickert, J.-H. Schulze, A. Strittmatter, M. Gschrey, S. Rodt, S. Reitzenstein, and T. Heindel, “Tools for the performance optimization of single-photon quantum key distribution,” [npj Quantum Information](#) **6** (2020).
- ⁵²D. Gottesman, H.-K. Lo, N. Lütkenhaus, and J. Preskill, “Security of quantum key distribution with imperfect devices,” [Quantum Info. Comput.](#) **4**, 325–360 (2004).
- ⁵³P. Chaiwongkhot, S. Sajeed, L. Lydersen, and V. Makarov, “Finite-key-size effect in a commercial plug-and-play QKD system,” [Quantum Science and Technology](#) **2**, 044003 (2017).
- ⁵⁴Note, that a more widely used term in the literature is quantum bit error rate (QBER) in units of s^{-1} . As the QBER entering the binary Shannon entropy in Eq. 1 (denoted as e) must be a probability (cf. Subsection III A), we consistently use the quantum bit error ratio, defined as the ratio of erroneous bits to all detected bits in our work.
- ⁵⁵L. Lydersen and J. Skaar, “Security of quantum key distribution with bit and basis dependent detector flaws.” [Quantum Information and Computation](#) **10**, 60–76 (2010).
- ⁵⁶P. Grünwald, “Effective second-order correlation function and single-photon detection,” [New Journal of Physics](#) **21**, 093003 (2019).
- ⁵⁷J. R. Chavez-Mackay, P. Grünwald, and B. M. Rodríguez-Lara, “Estimating the single-photon projection of low-intensity light sources,” [Physical Review A](#) **101**, 053815 (2020).

- ⁵⁸D. Rusca, A. Boaron, F. Grünenfelder, A. Martin, and H. Zbinden, “Finite-key analysis for the 1-decoy state qkd protocol,” *Applied Physics Letters* **112**, 171104 (2018).
- ⁵⁹C.-M. Lee, M. A. Buyukkaya, S. Aghaeimeibodi, A. Karasahin, C. J. K. Richardson, and E. Waks, “A fiber-integrated nanobeam single photon source emitting at telecom wavelengths,” *Applied Physics Letters* **114**, 171101 (2019).
- ⁶⁰N. Srocka, P. Mrowiński, J. Große, M. von Helversen, T. Heindel, S. Rodt, and S. Reitzenstein, “Deterministically fabricated quantum dot single-photon source emitting indistinguishable photons in the telecom o-band,” *Applied Physics Letters* **116**, 231104 (2020).
- ⁶¹S. Kolatschek, C. Nawrath, S. Bauer, J. Huang, J. Fischer, R. Sittig, M. Jetter, S. L. Portalupi, and P. Michler, “Bright purcell enhanced single-photon source in the telecom o-band based on a quantum dot in a circular bragg grating,” *Nano Letters* **21**, 7740–7745 (2021).
- ⁶²J.-P. Jahn, M. Munsch, L. Béguin, A. V. Kuhlmann, M. Renggli, Y. Huo, F. Ding, R. Trotta, M. Reindl, O. G. Schmidt, A. Rastelli, P. Treutlein, and R. J. Warburton, “An artificial rb atom in a semiconductor with lifetime-limited linewidth,” *Physical Review B* **92**, 245439 (2015).
- ⁶³C. Santori, M. Pelton, G. Solomon, Y. Dale, and Y. Yamamoto, “Triggered single photons from a quantum dot,” *Physical Review Letters* **86**, 1502 (2001).
- ⁶⁴L. Zhai, M. C. Löbl, G. N. Nguyen, J. Ritzmann, A. Javadi, C. Spinnler, A. D. Wieck, A. Ludwig, and R. J. Warburton, “Low-noise GaAs quantum dots for quantum photonics,” *Nature Communications* **11** (2020).
- ⁶⁵S. Nauerth, F. Moll, M. Rau, C. Fuchs, J. Horwath, S. Frick, and H. Weinfurter, “Air-to-ground quantum communication,” *Nature Photonics* **7**, 382–386 (2013).
- ⁶⁶S.-K. Liao, W.-Q. Cai, W.-Y. Liu, L. Zhang, Y. Li, J.-G. Ren, J. Yin, Q. Shen, Y. Cao, Z.-P. Li, F.-Z. Li, X.-W. Chen, L.-H. Sun, J.-J. Jia, J.-C. Wu, X.-J. Jiang, J.-F. Wang, Y.-M. Huang, Q. Wang, Y.-L. Zhou, L. Deng, T. Xi, L. Ma, T. Hu, Q. Zhang, Y.-A. Chen, N.-L. Liu, X.-B. Wang, Z.-C. Zhu, C.-Y. Lu, R. Shu, C.-Z. Peng, J.-Y. Wang, and J.-W. Pan, “Satellite-to-ground quantum key distribution,” *Nature* **549**, 43–47 (2017).
- ⁶⁷J. Yin, Y. Cao, Y.-H. Li, J.-G. Ren, S.-K. Liao, L. Zhang, W.-Q. Cai, W.-Y. Liu, B. Li, H. Dai, M. Li, Y.-M. Huang, L. Deng, L. Li, Q. Zhang, N.-L. Liu, Y.-A. Chen, C.-Y. Lu, R. Shu, C.-Z. Peng, J.-Y. Wang, and J.-W. Pan, “Satellite-to-ground entanglement-based quantum key distribution,” *Physical Review Letters* **119** (2017).

- ⁶⁸J. Yin, Y.-H. Li, S.-K. Liao, M. Yang, Y. Cao, L. Zhang, J.-G. Ren, W.-Q. Cai, W.-Y. Liu, S.-L. Li, R. Shu, Y.-M. Huang, L. Deng, L. Li, Q. Zhang, N.-L. Liu, Y.-A. Chen, C.-Y. Lu, X.-B. Wang, F. Xu, J.-Y. Wang, C.-Z. Peng, A. K. Ekert, and J.-W. Pan, “Entanglement-based secure quantum cryptography over 1,120 kilometres,” *Nature* **582**, 501–505 (2020).
- ⁶⁹R. Y. Q. Cai and V. Scarani, “Finite-key analysis for practical implementations of quantum key distribution,” *New Journal of Physics* **11**, 045024 (2009).
- ⁷⁰L. Rickert, T. Kupko, S. Rodt, S. Reitzenstein, and T. Heindel, “Optimized designs for telecom-wavelength quantum light sources based on hybrid circular bragg gratings,” *Optics Express* **27**, 36824 (2019).
- ⁷¹A. C. Dada, T. S. Santana, R. N. E. Malein, A. Koutroumanis, Y. Ma, J. M. Zajac, J. Y. Lim, J. D. Song, and B. D. Gerardot, “Indistinguishable single photons with flexible electronic triggering,” *Optica* **3**, 493–498 (2016).
- ⁷²P. Munnely, T. Heindel, A. Thoma, M. Kamp, S. Höfling, C. Schneider, and S. Reitzenstein, “Electrically tunable single-photon source triggered by a monolithically integrated quantum dot microlaser,” *ACS Photonics* **4**, 790–794 (2017).
- ⁷³J. P. Lee, E. Murray, A. J. Bennett, D. J. P. Ellis, C. Dangel, I. Farrer, P. Spencer, D. A. Ritchie, and A. J. Shields, “Electrically driven and electrically tunable quantum light sources,” *Applied Physics Letters* **110**, 071102 (2017).
- ⁷⁴Z.-H. Xiang, J. Huwer, J. Skiba-Szymanska, R. M. Stevenson, D. J. P. Ellis, I. Farrer, M. B. Ward, D. A. Ritchie, and A. J. Shields, “A tuneable telecom wavelength entangled light emitting diode deployed in an installed fibre network,” *Communications Physics* **3**, 121 (2020).
- ⁷⁵A. Thoma, P. Schnauber, M. Gschrey, M. Seifried, J. Wolters, J.-H. Schulze, A. Strittmatter, S. Rodt, A. Carmele, A. Knorr, T. Heindel, and S. Reitzenstein, “Exploring dephasing of a solid-state quantum emitter via time- and temperature-dependent hong-ou-mandel experiments,” *Physical Review Letters* **116**, 033601 (2016).
- ⁷⁶S. L. Braunstein and S. Pirandola, “Side-channel-free quantum key distribution,” *Physical Review Letters* **108**, 130502 (2012).
- ⁷⁷H.-K. Lo, M. Curty, and B. Qi, “Measurement-device-independent quantum key distribution,” *Physical Review Letters* **108**, 130503 (2012).

SUPPLEMENTAL MATERIAL

A. Blinking behavior

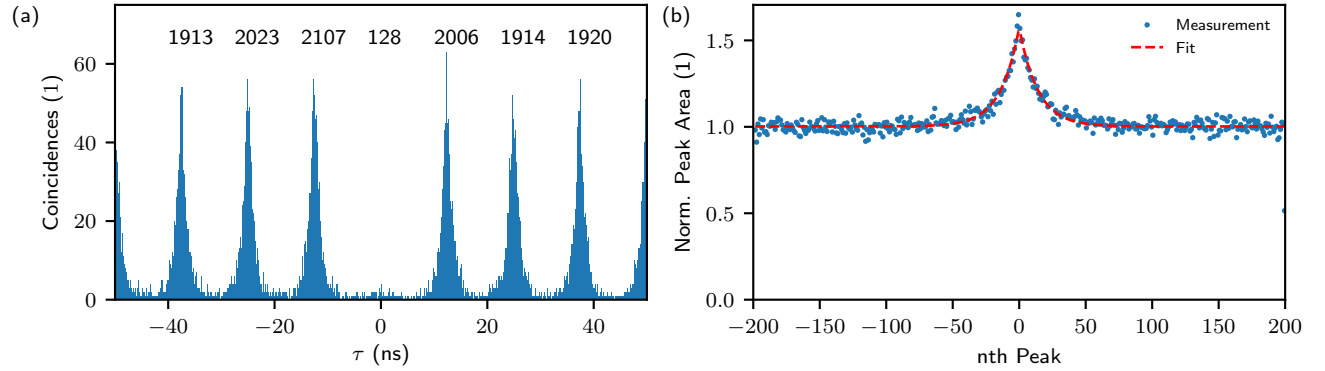


FIG. S1. Second-order autocorrelation $g^{(2)}(\tau)$ histogram (50 ps bin width) under pulsed resonant p-shell excitation at 1247.9 nm. (a) Histogram from Fig. 2 (b) in the main text with the number of integrated coincidences shown for each peak. (b) Normalized number of integrated coincidences of the peaks in a wider temporal window revealing blinking behavior of the quantum dot. The time constants $\tau_{\text{on}} = (482.3 \pm 2.5)$ ns and $\tau_{\text{off}} = (275.1 \pm 1.0)$ ns are extracted from the model-fit following Ref.⁶³.

B. Measurement data for QBER and signal fraction under temporal filtering

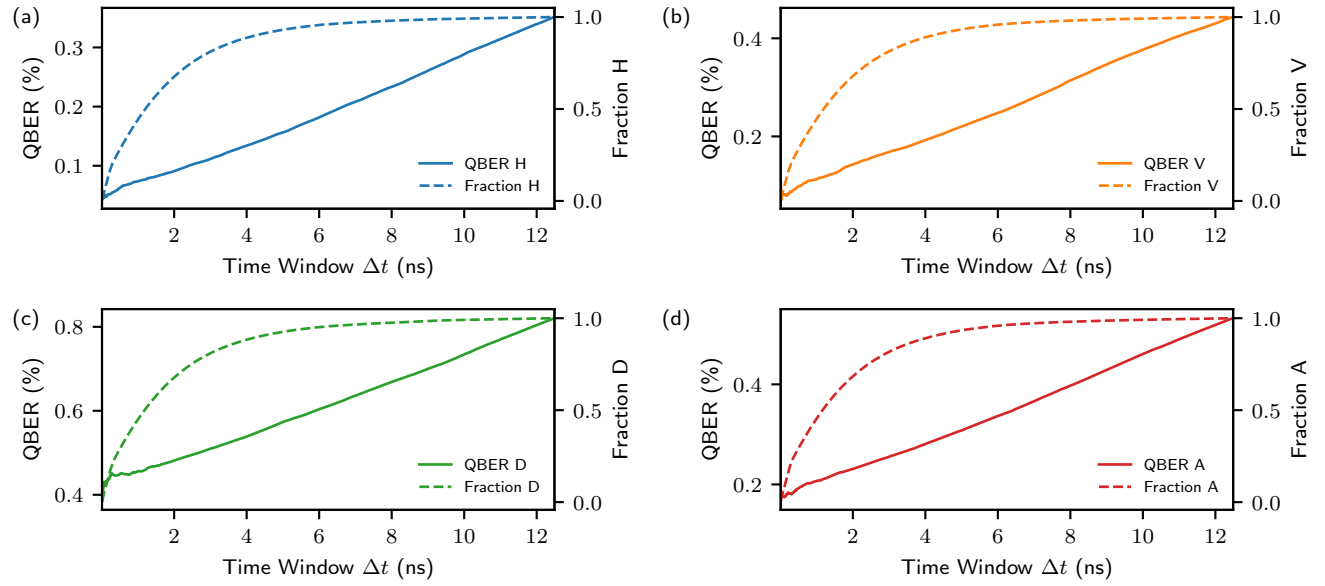


FIG. S2. The effect of temporal filtering on the QBER and Fraction of the overall signal for each polarization. From the photon arrival time distributions of Fig. 2 (a) in the main text the QBERs for all four possible input polarizations are calculated. See Ref. [51](#) for detailed explanations.

C. Parameter Optimization

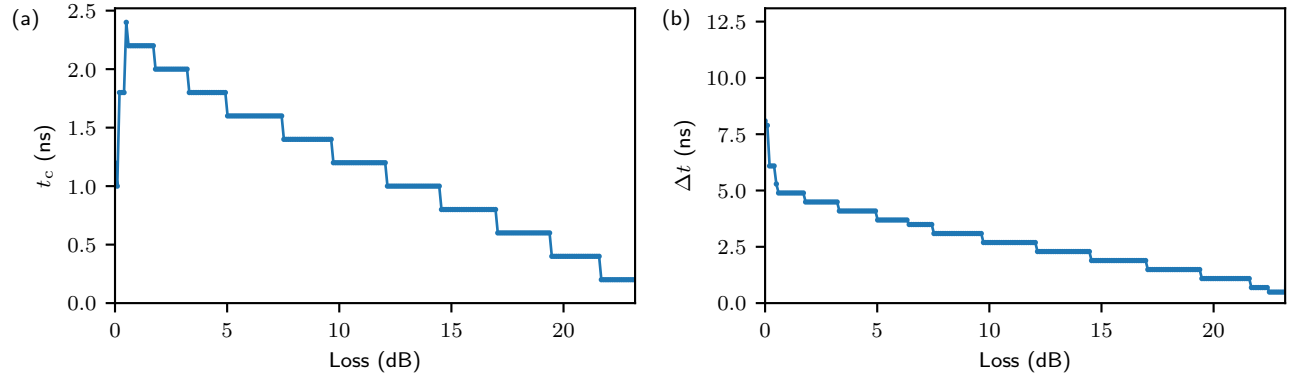


FIG. S3. Parameter sets for (a) center t_c and (b) width Δ_t of the 2D temporal filters optimized for different losses underlying the asymptotic key rate in Fig. 4 (a) of the main text (data displayed by points, lines are a guide to the eye). The value of t_c reduces with decreasing Δ_t , i.e. the optimal signal to noise ratio can be achieved around the maximum of the photon arrival time distribution. The step-like behavior results from the finite statistics of the data and the finite step size for optimization.